Remote nucleation and stationary domain walls via transition waves in tristable magnetoelastic lattices

Anusree Ray ●,[*] Samanvay Anand ●,[*] Vivekanand Dabade,[†] and Rajesh Chaunsali ●[‡]

Department of Aerospace Engineering, Indian Institute of Science, Bangalore 560012, India

We present a magnetoelastic lattice in which a localized external magnetic field, generated by an assembly of fixed magnets, tunes the potential landscape to create monostable, bistable, and tristable configurations. Focusing on the tristable potential, we numerically and experimentally confirm the existence of three distinct types of transition waves, each characterized by unique amplitudes and velocities, and establish a scaling law that governs their behavior. We also examine how these transition waves interact with the system's finite boundaries. Furthermore, by adjusting the potential symmetry through the localized external field, we investigate wave collision dynamics. In lattices with asymmetric potentials, the collision of similar transition waves leads to the remote nucleation of a third phase. In symmetric potentials, the collision of dissimilar transition waves results in the formation of a stationary domain wall, with its width tuned by the shape of the tristable potential well.

I. INTRODUCTION

Transition waves play a crucial role in various material processes, such as dislocation dynamics, where defects propagate through crystal lattices [1], and phase transitions in advanced materials such as ferroelectrics [2], ferromagnets [3], and shape memory alloys [4]. These waves are characterized by moving boundaries, referred to as phase boundaries or domain walls, which separate regions where the material exists in different phases. As the transition wave propagates, these boundaries shift, causing material elements to switch from one phase to another. Extensive theoretical studies have explored these waves in systems with nonconvex energy landscapes, where multiple stable equilibria exist, driving the sequential transition of elements from one equilibrium state to another [5–13].

Similar phenomena have emerged in metamaterials in recent years, where macroscopic mechanical systems exhibit multiple stable equilibria [14,15]. By finely adjusting potentials and degrees of freedom, precise control over transition waves is achieved in metamaterials, enabling the design of reconfigurable structures with applications in soft robotics [16,17], energy absorption [18], deployable structures [19], and sound control [20,21].

Initially, research into transition waves in metamaterials primarily focused on bistable unit cells with asymmetry sufficient to compensate for the system damping and make the transition wave sustainable [22–27]. However, recent developments have expanded this design space by integrating magnetic elements into metamaterial lattices, enabling the realization of systems with more than two stable equilibria [28,29]. This has led to novel observations, such as the

formation of stationary domain walls through the collision of two transition waves [28], a mechanism distinct from bistable lattices, which require additional defects to achieve similar outcomes [30,31]. Furthermore, magnetic elements enable *in situ* tuning of the system's potential energy landscape using an external magnetic field, without requiring physical changes to the lattice geometry. This provides more precise control over transition wave propagation and facilitates the creation of more adaptable and functional designs [32].

Despite these advancements, a systematic design strategy for creating metamaterials with multiple stable equilibria using only external magnetic fields is still lacking. Such systems could allow for real-time tuning of the potential landscape—whether monostable, bistable, or tristable—without requiring changes to the metamaterial's geometry. This flexibility would support a wide range of wave dynamics. Notably, wave behavior in tristable configurations remains underexplored in the literature. Key open questions include the following: (1) How many types of transition waves can such lattices support, and is there a universal law governing their characteristics? (2) How do these waves interact with finite boundaries? (3) What happens when different transition waves collide?

In this work, we demonstrate how a localized external magnetic field, generated by an assembly of permanent magnets, can tune the potential landscape of a metamaterial lattice, enabling monostable, bistable, and tristable behavior. We focus on the tristable configuration, where experimental observations reveal the existence of three distinct transition waves. We validate with experiments a scaling law relating wave velocity to power dissipation, as theoretically predicted in earlier studies [33]. Additionally, we investigate how boundary conditions affect these transition waves.

We further explore the collision dynamics of transition waves in both symmetric and asymmetric potentials, adjustable via the localized magnetic field. For asymmetric potentials, we show that two transition waves initiated from opposite ends collide, nucleating a third phase. Finally, for

---

*These authors contributed equally to this work.
†Contact author: dabade@iisc.ac.in
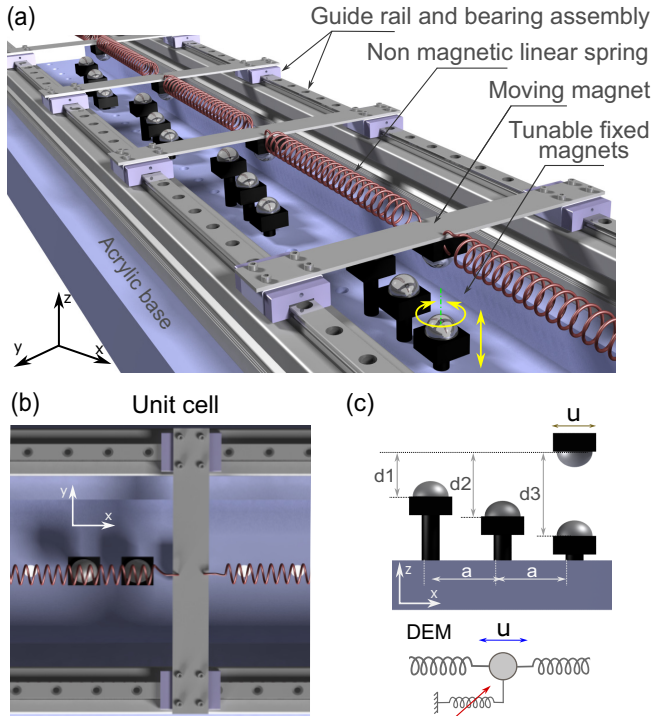‡Contact author: rchaunsali@iisc.ac.in

FIG. 1. Experimental setup. (a) One-dimensional lattice assembly where the on-site potential is induced by fixed magnets. Moving masses are the sliding beams. (b) Top view of the unit cell, comprising three fixed magnets and one moving magnet attached beneath the sliding beam. (c) As per the discrete element model (DEM), the depths of the fixed magnets (d_1, d_2, and d_3) create a multistable on-site potential for the moving magnet.

symmetric potentials, we experimentally demonstrate that the collision of two transition waves results in the formation of a stationary domain wall. Our findings reveal a previously unexplored correlation between the width of the domain wall

and that of the colliding transition waves, governed by the shape of the tristable potential.

II. EXPERIMENTAL SETUP

We design a lattice comprising ten unit cells, each consisting of a sliding beam (aluminum) connected to its neighbors via axial springs (phosphor bronze), as depicted in Fig. 1. The structure rests on a solid acrylic base supported by a pair of aluminum extrusions, housing the linear guide rail and bearing assembly (MGN7C, HIWIN). Underneath each beam is a Neodymium (N-52) permanent magnet, referred to as a "moving magnet," as it moves along the x axis with the beam. Three magnets are affixed to the acrylic base for each unit cell, spaced at a distance $a = 20$ mm between them. All the permanent magnets are spherical of a radius of $r = 5$ mm and uniformly magnetized along the out-of-plane direction (z axis). The unit cells are adequately spaced, with a distance $l = 120$ mm between them, ensuring that the moving magnets primarily interact with the three fixed magnets within their respective unit cells. By individually rotating the fixed magnets, we alter their depths (d_1, d_2, and d_3) and change the localized magnetic field, thus adjusting the effective on-site potential experienced by the moving magnet. For the measurements, we employ a laser Doppler vibrometer (Polytec single-point LDV) to detect the displacement of each moving mass.

III. NUMERICAL MODELING

A. Nonlinear on-site potential

First, we model the magnetic interaction between moving and stationary magnets within a unit cell. Since all magnets possess uniform magnetization m_s and are spherical with radius r, we derive the interaction energy, a function of u, the axial displacement of the moving mass, using Maxwell's equations [refer to Supplemental Material [34] (Sec. I) and also Refs. [35,36] therein for details]:

$$E(u) = \frac{4\pi m_s^2}{9\mu_0} r^6 \left[\left(\frac{1}{[(u+a)^2 + d_1^2]^{3/2}} - \frac{3d_1^2}{[(u+a)^2 + d_1^2]^{5/2}} \right) + \left(\frac{1}{(u^2 + d_2^2)^{3/2}} - \frac{3d_2^2}{(u^2 + d_2^2)^{5/2}} \right) \right.$$
$$\left. + \left(\frac{1}{[(u-a)^2 + d_3^2]^{3/2}} - \frac{3d_3^2}{[(u-a)^2 + d_3^2]^{5/2}} \right) \right],$$

(1)

where $\mu_0 = 4\pi \times 10^{-7}$ Vs/Am denotes vacuum permeability. The magnetization of all N-52 magnets is considered as $m_s = 0.8$ T. Additionally, the depths of fixed magnets d_1, d_2, and d_3 are adjustable to modify the interaction energy landscape, as illustrated in Fig. 2. We maintain d_2 constant and examine the energy landscape's behavior as d_1 and d_3 vary. Figure 2(a) demonstrates the possibility of monostable, bistable, and tristable potential landscapes for various depth combinations. We focus on the tristable regime, presenting two distinct tristable landscapes, one asymmetric and the other symmetric about $u = 0$, depicted in Figs. 2(b) and 2(c), respectively. In the later sections, we will analyze transition waves that facilitate system switching across three differ-

ent phases (corresponding to three local minima), namely, Phase 1, Phase 2, and Phase 3.

B. Equations of motion

We employ the discrete element method (DEM) to simulate the dynamics of our system. Sliding beams with moving magnets are treated as lumped masses interconnected by linear springs. To simplify calculations, we assume a significantly higher bending rigidity for the beams, neglecting out-of-plane motion along the z axis for the moving mass. The derivative of the nonconvex on-site energy, previously calculated, serves as a measure of the on-site force acting on the moving magnets.
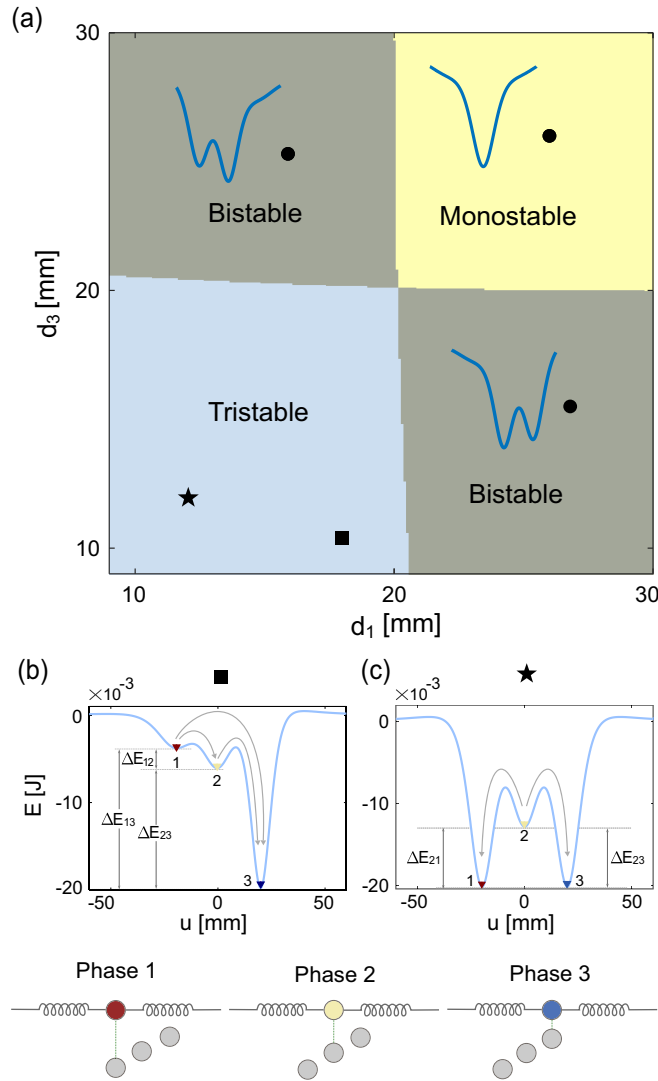
FIG. 2. (a) Phase diagram of the on-site potential as a function of d_1 and d_3, for fixed $a = 20$ mm and $d_2 = 15.3$ mm. (b) Asymmetric tristable on-site potential considered for the experiment, $(d_1, d_3) = (18, 10.4)$ mm. (c) Symmetric tristable on-site potential considered for the experiment $(d_1, d_3) = (12, 12)$ mm. Energy differences between different stable states are highlighted. Arrows denote different types of transition waves between Phase 1, Phase 2, and Phase 3.

Consequently, the equation of motion for the nth unit cell is given by

$$mu_{n,tt} - k(u_{n-1} - 2u_n + u_{n+1}) + E'(u_n)$$
$$- c_1(u_{(n-1),t} - 2u_{n,t} + u_{(n+1),t}) + c_2\text{sgn}(u_{n,t}) = 0, \quad (2)$$

where m represents the mass of the moving assembly, k denotes the linear stiffness of the springs, and c_1 and c_2 are intersite and on-site damping parameters, respectively. Variables following a comma in indices denote partial derivatives. As the moving mass slides on the guide rails, we utilize a dry friction damping model for the on-site term and a viscous damping model for the springs.

C. Scaling law for transition wave

In this section, we derive the scaling law for transition waves propagating in the system with velocity v. We thus assume $u_n(t) = u(nl - vt) \equiv u(\xi)$ and substitute it into Eq. (2) to yield

$$mv^2 u_{,\xi\xi} - k(u(\xi - l) - 2u(\xi) + u(\xi + l))$$
$$+ E'(u) + c_1 v[u_{,\xi}(\xi - l) - 2u_{,\xi}(\xi) + u_{,\xi}(\xi + l)]$$
$$- c_2 v \, \text{sgn}(u_{,\xi}) = 0. \quad (3)$$

Equations are thus transformed into a traveling frame of reference ξ. Multiplying Eq. (3) by $u_{,\xi}$ and integrating over the real ξ axis, we obtain

$$\int_{-\infty}^{\infty} [mv^2 u_{,\xi\xi} - k(u(\xi - l) - 2u(\xi) + u(\xi + l))$$
$$+ E'(u) + c_1 v(u_{,\xi}(\xi - l) - 2u_{,\xi}(\xi) + u_{,\xi}(\xi + l))$$
$$- c_2 v \, \text{sgn}(u_{,\xi})]u_{,\xi}d\xi = 0. \quad (4)$$

If the transition wave changes the system from the initial phase u_i at $t \to -\infty$ ($\xi \to \infty$) to u_f at $t \to \infty$ ($\xi \to -\infty$), we impose $u(\xi \to \infty) = u_i$ and $u(\xi \to -\infty) = u_f$. Furthermore, for a dissipative system, the wave profile would reach a steady state at $t \to \infty$, implying $u_{,\xi}(\xi \to -\infty) = 0$. Since the system was initially at rest, we also have $u_{,\xi}(\xi \to \infty) = 0$. Upon examining the individual integrals in Eq. (4), we find

$$\int_{-\infty}^{\infty} (mv^2 u_{,\xi\xi})u_{,\xi}d\xi = \int_{-\infty}^{\infty} \frac{mv^2}{2}\frac{d}{d\xi}(u_{,\xi})^2 d\xi = 0. \quad (5)$$

Next we compute the integral

$$\mathcal{I} = \int_{-\infty}^{\infty} \{k[u(\xi - l) - 2u(\xi) + u(\xi + l)]\}u_{,\xi}d\xi.$$

The second term of $\mathcal{I}$ reduced as

$$-2k\int_{-\infty}^{\infty} u(\xi)u_{,\xi}d\xi$$
$$= -k\int_{-\infty}^{\infty} \frac{d}{d\xi}(u(\xi))^2 d\xi = -k(u_i^2 - u_f^2). \quad (6)$$

We define $\eta = \xi - l$ and subsequently the first term of $\mathcal{I}$ can be rewritten as

$$\int_{-\infty}^{\infty} ku(\xi - l)u_{,\xi}(\xi)d\xi = \int_{-\infty}^{\infty} ku(\eta)u_{,\eta}(\eta + l)d\eta. \quad (7)$$

Since η is a dummy variable, this can be rewritten as

$$\int_{-\infty}^{\infty} ku(\eta)u_{,\eta}(\eta + l)d\eta = \int_{-\infty}^{\infty} ku(\xi)u_{,\xi}(\xi + l)d\xi. \quad (8)$$

Therefore, the first and third terms of $\mathcal{I}$ are deduced to

$$\int_{-\infty}^{\infty} \{k[u(\xi - l) + (\xi + l)]\}u_{,\xi}d\xi$$
$$= k\int_{-\infty}^{\infty} [u(\xi)u_{,\xi}(\xi + l) + u(\xi + l)u_{,\xi}(\xi)]d\xi$$
$$= k\int_{-\infty}^{\infty} \frac{d}{d\xi}[u(\xi)u(\xi + l)] = k(u_i^2 - u_f^2). \quad (9)$$

Combining Eqs. (6) and (9), the integral $\mathcal{I} = 0$. Finally, the term in Eq. (4)

$$\int_{-\infty}^{\infty} E'(u)u_{,\xi}d\xi = E(u_i) - E(u_f) = \Delta E. \qquad (10)$$

Therefore Eq. (4) reduces to

$$\Delta E = \int_{-\infty}^{\infty} [-c_1 v(u_{,\xi}(\xi - l) - 2u_{,\xi}(\xi) + u_{,\xi}(\xi + l)) \\ + c_2 v \, \mathrm{sgn}(u_{,\xi})]u_{,\xi}d\xi. \qquad (11)$$

Multiplying both sides with v/l, approximating the right-hand side by a discrete system, we obtain

$$v\Delta e \simeq \sum_{n=1}^{N} [-c_1(u_{n-1,t} - 2u_{n,t} + u_{n+1,t}) \\ + c_2\mathrm{sgn}(u_{n,t})]u_{n,t} \equiv P_d, \qquad (12)$$

where $\Delta e \equiv \Delta E/l$ represents the change in on-site energy per unit length. The right-hand side denotes the total power dissipated (P_d) by viscous and Coulomb damping. Due to discreteness, P_d oscillates in time with a period $T = l/v$ [see Supplemental Material [34] (Sec. II) for details]. Therefore, we compute the time-averaged P_d as

$$\langle P_d \rangle = \frac{1}{T} \int_{t_0}^{t_0+T} P_d dt, \qquad (13)$$

and we modify the scaling law as

$$v\Delta e \simeq \langle P_d \rangle. \qquad (14)$$

A similar scaling law can be found in the work of Nadkarni *et al.* [33]. However, we have validated this prediction for the simultaneous presence of nonlinear on-site damping and linear intersite damping in our system. Since the power dissipated on the right-hand side is always positive due to the second law, we can conclude that $v\Delta e \geqslant 0$, which is analogous to the entropy condition derived in Ref. [7], with Δe acting as the driving force on the phase boundary propagation. In our tristable lattice, the scaling remains independent of interparticle stiffness. Furthermore, the specific topology of the on-site potential does not affect the scaling law; instead, it depends on the initial and final configuration of the energy state.

IV. RESULTS AND DISCUSSIONS

In this section, we focus on tristable configurations and present both numerical and experimental results addressing four key aspects: (1) the formation of transition waves, (2) the influence of boundary conditions, (3) nucleation behavior, and (4) the existence of stationary domain walls.

A. Formation of transition waves

We perform experiments on a chain comprising ten unit cells with an asymmetric tristable on-site potential, as depicted in Fig. 2(b). Due to asymmetry in the well, we expect several sustainable transition waves propagating in the lattice. These wave profiles are also referred to as *kinks* or *antikinks* [37], and manifest as localized wave packets propagating with

a constant shape. We identify three distinct types of transition waves: (i) $1 \rightarrow 2$, with the transition from Phase 1 to Phase 2; (ii) $2 \rightarrow 3$, with the transition from Phase 2 to Phase 3; and (iii) $1 \rightarrow 3$, with the transition from Phase 1 to Phase 3. Note that transition waves, such as $3 \rightarrow 1$, $3 \rightarrow 2$, or $2 \rightarrow 1$, are energetically not favorable as the final state is at higher energy, which enhances the effect of dissipation and leads to the absence of a sustainable transition wave [14].

First, we consider a scenario where all unit cells are in the highest energy state, i.e., Phase 1, and both ends of the chain are fixed. We rely on prestraining the first spring and releasing its strain energy so that we can initiate the transition wave in a controlled and repeatable manner. The prestrain is introduced by snapping the first unit cell into Phase 2 and fixing it in place while restraining the second unit cell, causing the spring between them to develop compressive strain. When the second unit cell is released, the transition wave is initiated. We observe a large-amplitude nonlinear wave propagating through the lattice, transitioning each unit cell from Phase 1 to Phase 2 as shown in Fig. 3(a). The spatiotemporal map of the displacement is plotted in Fig. 3(b), clearly indicating the propagation of the $1 \rightarrow 2$ transition wave. Similarly, we conduct experiments and observe $2 \rightarrow 3$ and $1 \rightarrow 3$ transition waves as shown in Figs. 3(c) and 3(d), respectively. We also conduct numerical simulations on longer chains with 100 unit cells [see Supplemental Material [34] (Sec. II) for details]. We confirm that all types of transition waves are sustainable in these longer chains. This further demonstrates the fact that the asymmetries in the potential wells lead to energy gain after each snapping of unit cells, which compensates for the energy lost due to damping and thus facilitates a sustainable propagation of transition waves [23,28].

Furthermore, experimental data is utilized to fine-tune the damping parameters of the numerical model, with values of c_1 as 0.05, 0.1, and 0.001 N s/m, and c_2 as 0.11, 0.13, and 0.2 N for $1 \rightarrow 2$, $2 \rightarrow 3$, and $1 \rightarrow 3$ transition waves, respectively. The insets of Figs. 3(b)–3(d) show the comparison of temporal dynamics measured experimentally and modeled numerically.

From Figs. 3(b)–3(d), we observe that the $1 \rightarrow 2$, $2 \rightarrow 3$, and $1 \rightarrow 3$ transition waves reach the end of the chain at approximately 0.32, 0.42, and 0.27 s, respectively. This means that the $1 \rightarrow 3$ transition wave has the highest velocity, while the $2 \rightarrow 3$ transition wave has the lowest. This can be explained using the scaling law derived in Eq. (14), which relates the velocity of a transition wave (v) to the dissipated power ($\langle P_d \rangle$) and the energy difference (Δe) in the on-site potential. In Fig. 3(e), we plot $\langle P_d \rangle$ against $v\Delta e$ from both experimental and numerical results. The data points lie on a straight line with slope 1, confirming the validity of the scaling law. In our system, the power dissipated by the different transition waves follows the order $\langle P_d \rangle_{1 \rightarrow 3} > \langle P_d \rangle_{2 \rightarrow 3} > \langle P_d \rangle_{1 \rightarrow 2}$. However, the energy difference also follows the relation $\Delta e_{1 \rightarrow 3} > \Delta e_{2 \rightarrow 3} > \Delta e_{1 \rightarrow 2}$. Consequently, the wave velocity (v), which depends on the ratio $\langle P_d \rangle / \Delta e$, follows the order $v_{1 \rightarrow 3} > v_{1 \rightarrow 2} > v_{2 \rightarrow 3}$ for this particular setup.

To the best of the authors' knowledge, the $1 \rightarrow 3$ transition wave, which progresses directly from Phase 1 to Phase 3 without stabilizing at the intermediate state, has not been previously documented in the literature. We further
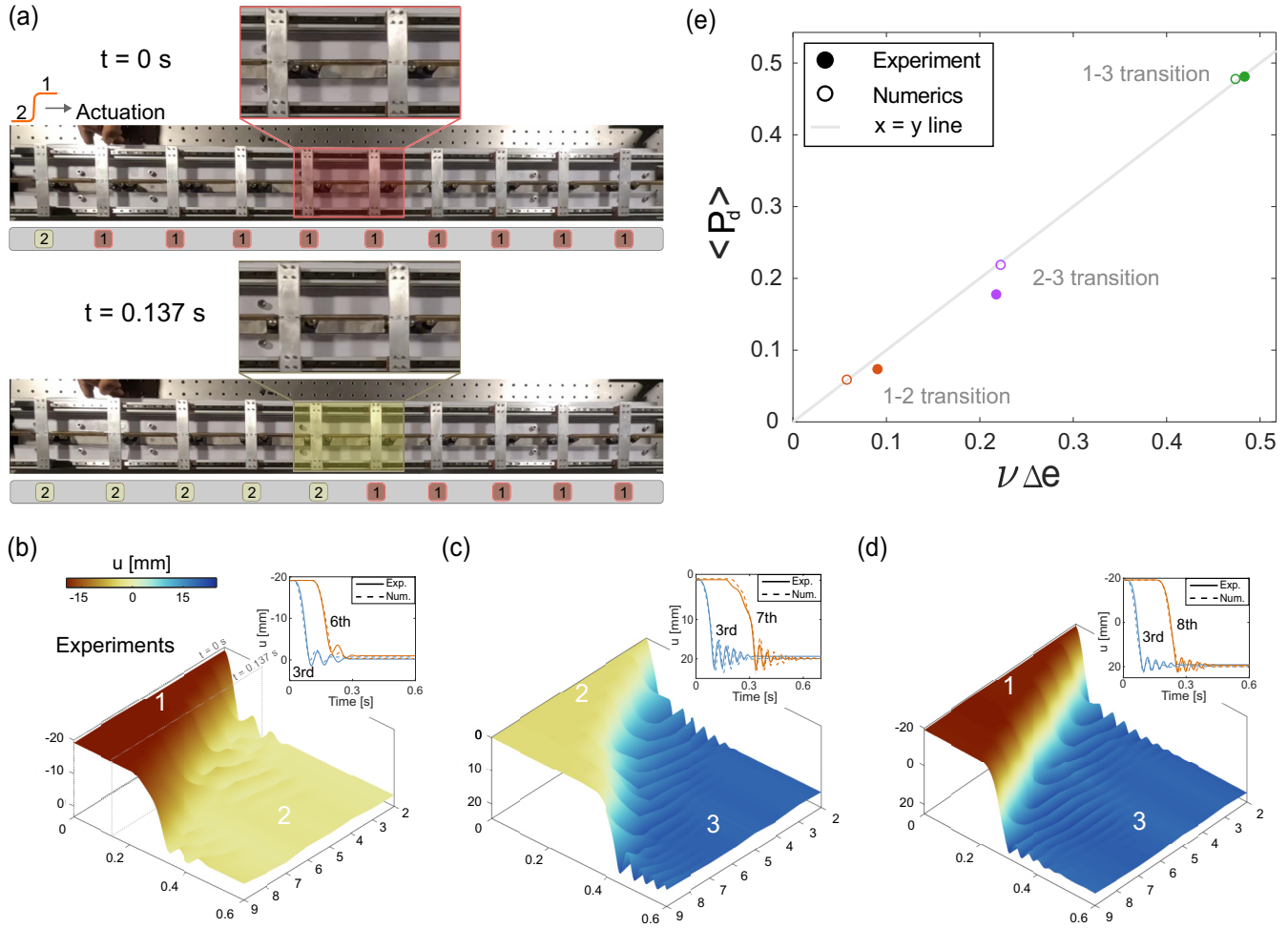
FIG. 3. Three types of transition waves. (a) Snapshots from experiments demonstrating the $1 \rightarrow 2$ transition wave. The unit cells are labeled with the phases. (b)–(d) Spatiotemporal plots of displacement obtained from experiments for $1 \rightarrow 2$, $2 \rightarrow 3$, and $1 \rightarrow 3$ transition waves, respectively. Insets show the displacement time series of different moving masses. (e) Experimental validation of the scaling law in Eq. (14).

investigate this unique transition wave by varying the onsite potential and excitation amplitude. First, we keep d_1 and d_2 constant while varying d_3 to control the energy of Phase 3 relative to Phases 1 and 2, while maintaining nearly constant energy barriers, as shown in Fig. 4(a). As d_3 increases, the
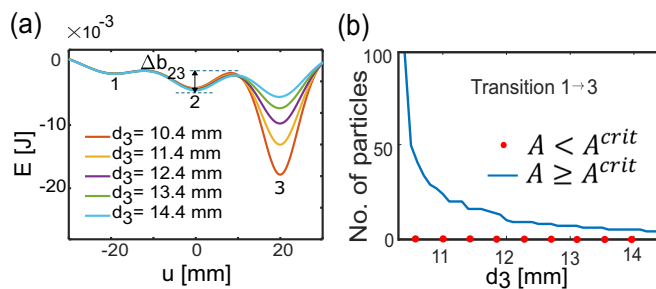

FIG. 4. (a) On-site potential for varying values of d_3 keeping $d_1 = 18$ mm and $d_2 = 15.3$ mm, fixed. (b) Number of particles undergoing the $1 \rightarrow 3$ transition in a chain of length 100 vs d_3. The $1 \rightarrow 3$ transition is dependent on the initial amplitude A. For all initial amplitudes less than A^{crit} ($= 32$ mm), we do not observe the $1 \rightarrow 3$ transition wave.

third well becomes shallower, reducing the asymmetry and lowering the energy differences ΔE_{13} and ΔE_{23}. Next, we conduct numerical simulations on a system of 100 unit cells with varying d_3 to examine the propagation length of the transition wave. When the initial amplitude exceeds the critical threshold to cross the energy barrier between Phase 2 and Phase 3 ($A^{\mathrm{crit}} = 32$ mm), we observe the $1 \rightarrow 3$ transition wave propagating through the system as shown in Fig. 4(b). However, for larger values of d_3, fewer particles participate in the wave propagation, suggesting that reduced asymmetry of Phase 3 with Phases 1 and 2 results in lower energy gain with each snap, thereby shortening the propagation distance.

B. Effect of boundary conditions

In this section, we evaluate the role of boundary conditions on the behavior of transition waves. All of our previous studies have been conducted on chains with fixed-fixed boundary conditions, where we observed no reflection of transition waves upon reaching the opposite end of the chain. To assess whether this observed behavior persists under varying boundary conditions, we analyze a chain of 100 unit cells with a distinct
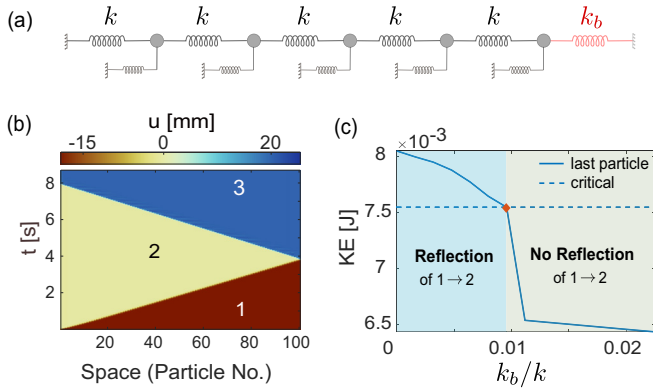
FIG. 5. (a) Schematic of a chain with different stiffness (k_b) at the right boundary. (b) Spatiotemporal plot of displacement indicating reflection of the $1 \to 2$ transition wave from the free (right) end. (c) Kinetic energy (KE) vs normalized stiffness. The red marker represents the maximum normalized stiffness (k_b/k) at which a reflected transition wave can occur. The blue and green regions indicate the range of stiffness corresponding to the presence or absence of the reflected transition wave.

stiffness, k_b, applied only to the final spring in the chain, as depicted in Fig. 5(a). The interparticle stiffness for all other springs remains k. We conduct a numerical study on the reflection of transition waves as a function of k_b. For instance, $k_b = 0$ corresponds to a free boundary condition. The spatiotemporal plot of displacement for this case is shown in Fig. 5(b). We observe a $1 \to 2$ transition wave propagating from left to right, converting the entire chain into Phase 2. Upon reaching the free boundary at the right end, a reflected $2 \to 3$ transition wave initiates, converting the chain from Phase 2 to Phase 3, the lowest energy state. Notably, no reflection occurs when $2 \to 3$ or $1 \to 3$ transition waves approach the free boundary, as the chain has already reached its most stable state (Phase 3) by this point, with no lower energy states available.

Next, we investigate wave reflection in chains with varying values of k_b. Our results show that the $1 \to 2$ transition wave reflects as a $2 \to 3$ wave when $k_b/k < 0.0096$. This threshold is explained by tracking the peak kinetic energy of the last particle, comparing it to the effective energy barrier necessary to transition to the lower energy state, Phase 3. Figure 5(c) illustrates the peak kinetic energy as a function of the normalized stiffness k_b/k alongside the critical kinetic energy required for the $2 \to 3$ transition. This critical kinetic energy, derived from simulations of the $2 \to 3$ wave in the chain's bulk under identical parameters, is given as $\mathrm{KE}_{2\to3}^{\mathrm{crit}} = 3.18 \times \Delta b_{23}$, where Δb_{23} represents the energy barrier between Phase 2 and Phase 3, with the factor of 3.18 capturing interparticle stiffness and on-site potential asymmetry effects. Our findings indicate that reflection occurs when the peak kinetic energy of the last particle surpasses this critical threshold. These insights open avenues for manipulating the final state of a multistable lattice through boundary condition adjustments.

C. Nucleation

In this section, we study the collision of two transition waves. We consider a chain with an asymmetric tristable on-site potential shown in Fig. 2(b) and excite the chain from

both ends. Initially, the entire chain is in Phase 1. We then trigger $1 \to 2$ transition waves from both ends. We observe transition waves propagating towards each other from the extreme ends and colliding at the middle of the chain at about $t = 0.254$ s, as shown in Fig. 6(a). The collision induces larger displacements and thereby nucleates a new phase, i.e., Phase 3, in the fifth and sixth unit cells. Consequently, this nucleus triggers $2 \to 3$ transition waves from the middle of the chain that propagate back to the boundaries.

In Fig. 6(b), we show an experimentally measured spatiotemporal map of displacement. The formation of a remote nucleus and the lattice transforming to Phase 3 is evident. We further show the temporal dynamics of the fourth and sixth unit cells in Fig. 6(c). We observe that the fourth unit cell transitions to Phase 2 ($u \approx 0$) before the sixth unit cell. However, the latter transitions to Phase 3 earlier than the fourth unit cell. This is consistent with the earlier observation that nucleation occurs at the fifth and sixth unit cells.

Nucleation can be interpreted as the collision of a kink and an antikink traveling in opposite directions [37]. In our study, the asymmetric tristable potential ensures that the propagation of these kinks and anti-kinks remains sustainable, even in longer chains and under damping [see Supplemental Material [34] (Sec. III)]. The experimental demonstration of this nucleation mechanism is another aspect of our work. Previous studies explored nucleation via collisions of vector solitons or breathers [29,38,39], which relied on only two stable states. In contrast, our mechanism leverages the design of all three stable states. Furthermore, the sustainability of transition waves in larger systems under damping highlights the robustness of this approach for achieving nucleation in extensive systems.

Next, we delve deeper into the nucleation mechanism to assess its resilience under the varying asymmetry of the tristable on-site potential. By keeping d_1 and d_2 constant and varying d_3, as shown in Fig. 4(a), we simulate the collision of $1 \to 2$ transition waves in a ten-particle chain. The focus is on the central particles (fifth and sixth), which must acquire sufficient kinetic energy to overcome the effective energy barrier between Phase 2 and Phase 3. During the collision, the spring connecting the fifth and sixth particles remains unstretched, allowing the effective energy barrier to be approximated using the effective potential. This potential combines the on-site energy [$E(u)$] of the fifth (or sixth) particle with the intersite energy ($\frac{1}{2}ku^2$) of the spring connecting it to the fourth (or seventh) particle, as shown in Fig. 7(a) and given as

$$\mathrm{Energy}_{\mathrm{effective}}^{2\to3} = E(u) + \tfrac{1}{2}ku^2. \tag{15}$$

The effective energy barrier is determined by calculating the local maximum of the effective potential. This maximum occurs at $u_{\mathrm{min}}^{2\to3} \approx 10.712$ mm, a point between Phase 2 and Phase 3. The barrier is then given as

$$\mathrm{Barrier}_{\mathrm{effective}}^{2\to3} = \left| E\left(u_{\mathrm{min}}^{2\to3}\right) - E(\mathrm{Phase\ 2}) \right| + \tfrac{1}{2}k\left(u_{\mathrm{min}}^{2\to3}\right)^2. \tag{16}$$

Figure 7(b) shows the variation of the effective energy barrier with d_3. Additionally, the kinetic energy of the fifth and sixth particles is plotted at the moment they reach Phase 2. Remarkably, the kinetic energy consistently exceeds the effective energy barrier, confirming that the fifth and sixth particles
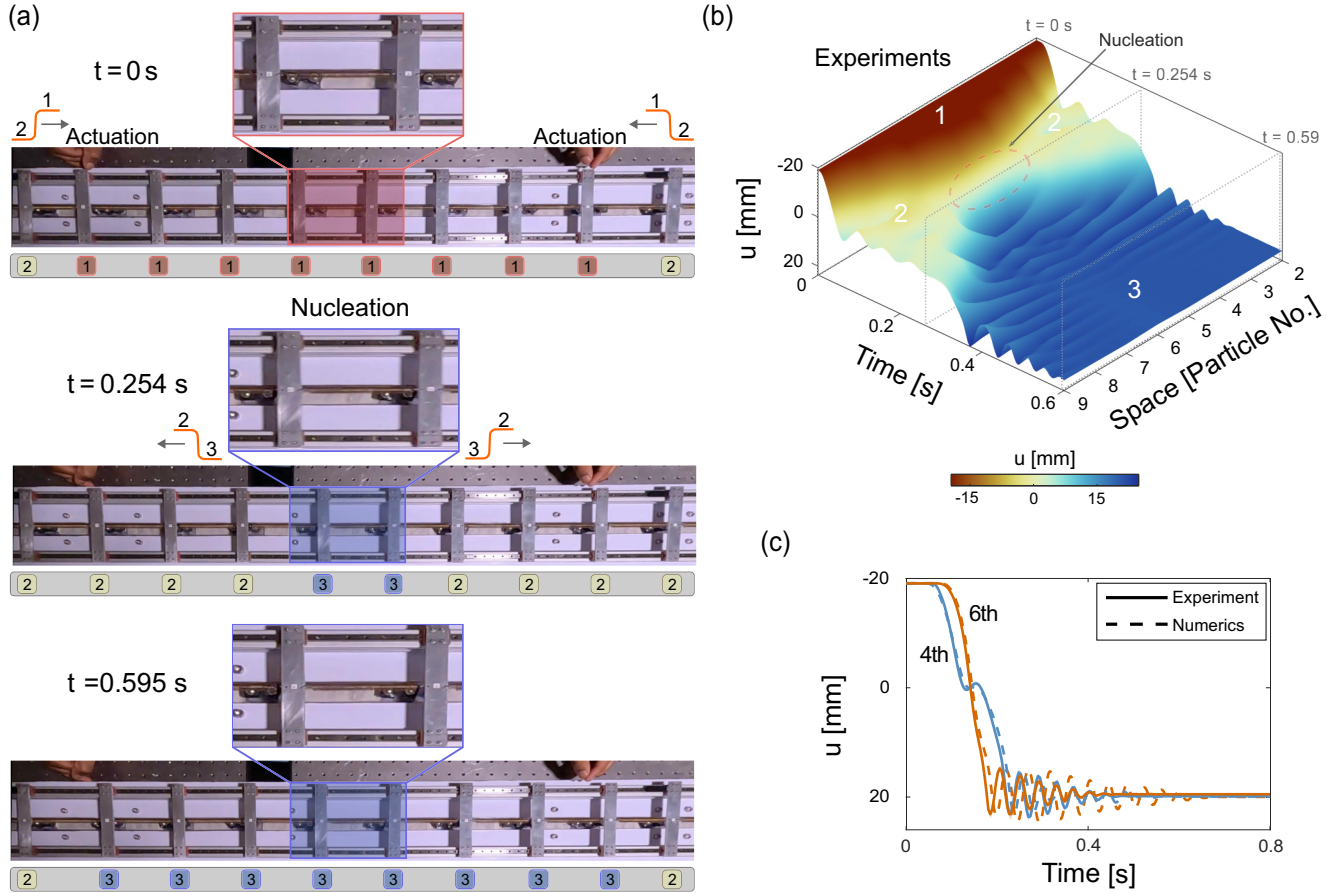
FIG. 6. Collision of two $1 \to 2$ transition waves nucleates a new phase, Phase 3. (a) Experimental snapshots highlighting the excitation and nucleation. The unit cells are labeled with the phases. (b) Spatiotemporal plot obtained from experiments showing the nucleation phenomena. The nucleus is formed at the fifth and sixth particles. (c) Displacement time series for the fourth and the sixth particles.

successfully reach Phase 3, thereby initiating nucleation for all tested values of d_3.

We also track the kinetic energy of the fifth or sixth particles immediately after nucleation, i.e., when they reach Phase 3, as shown in Fig. 7(b) as a function of d_3. For lower values of d_3 (corresponding to a deeper third well), this post-nucleation kinetic energy is significantly high, enabling the nucleation to propagate as a $2 \to 3$ transition wave toward the boundaries. However, for higher values of d_3, where Phase 2 and Phase 3 approach similar energy levels, nucleation occurs but fails to propagate toward the boundaries of the chain. This failure arises from the reduced kinetic energy of the nucleating particles post nucleation for large d_3.

To illustrate the effect of d_3 on the occurrence and propagation of nucleation, we present spatiotemporal displacement maps for two cases: $d_3 = 12.4$ mm and $d_3 = 14.4$ mm, in Figs. 7(c) and 7(d), respectively. The former demonstrates both nucleation and propagation, while the latter (with larger d_3) shows nucleation but no subsequent propagation. Nonetheless, nucleation and propagation are observed over a wide range of asymmetries between the stable states, as dictated by d_3.

Interestingly, the size of the nucleus depends on the number of particles in the chain. For example, two particles (the fifth and sixth) create the nucleus in the case above. Moreover, for

an odd number of particles in the chain, it is possible to have a nucleus of only one particle [see Supplemental Material [34] (Sec. III)]. This implies that even if only a single particle is nucleated due to the collision of a kink and an antikink, it can effectively induce the propagation of the new phase in both directions. Moreover, it is also possible to remotely nucleate a new phase at an arbitrary location (and not only at the center) in the chain using a time delay of actuation from either end [38]. Refer to Supplemental Material [34] (Sec. III) for details.

D. Stationary domain wall

In this section, we investigate the collision of two transition waves but with different on-site potentials. The tunability of our magnetoelastic lattice allows us to obtain a symmetric on-site potential well, as shown in Fig. 2(c). The difference in the energy levels of Phase 2 with Phase 1 and Phase 3 enables two different types of transition waves in the system. Initially, the whole lattice is kept in Phase 2. We trigger $2 \to 1$ and $2 \to 3$ transition waves from opposite ends and observe their collision. This scenario can also be understood as a collision of two kinks [37].

In Fig. 8(a), we observe two distinct propagating transition waves (moving domain walls) that collide at the center of the chain. However, the fifth and the sixth particles in the chain
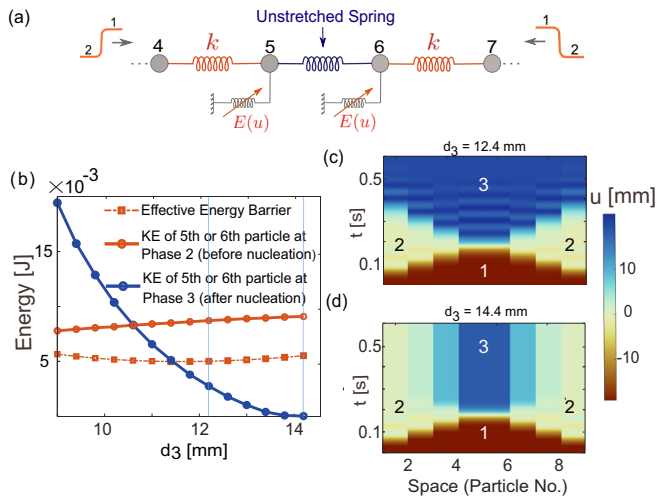
FIG. 7. (a) Schematic of the chain highlighting the region of collision of two $1 \rightarrow 2$ transition waves. (b) Energy vs d_3. The effective energy barrier is compared with the instantaneous kinetic energy of the fifth or sixth particles when they reach Phase 2. Moreover, the instantaneous kinetic energy of the fifth or sixth particles when they reach Phase 3 dictates the propagation after nucleation (blue curve). The vertical lines represent two cases: Case (i) $d_3 = 12.4$ mm and case (ii) $d_3 = 14.4$ mm, respectively. (c) and (d) Spatiotemporal plot of displacement for cases (i) and (ii), respectively.

continue to remain nearly in Phase 2, forming a stationary domain wall between Phase 1 and Phase 3. In Fig. 8(b), we show experimentally measured spatiotemporal maps of displacement confirming the formation of a stationary domain wall.

In Fig. 8(c), we plot the transient response of several particles in the chain. We observe that the fifth and the sixth particles remain stationary in that they do not snap to neighboring stable wells, forming a stationary domain wall; however, their equilibrium state is slightly perturbed from Phase 2 due to the coexistence of other states next to them. We also verify that stationary domain walls can form in longer chains. Moreover, the domain wall could be made of only one particle (with $u \approx 0$) if the chain consists of an odd number of particles. Refer to Supplemental Material [34] (Sec. IV) for details.

To further explore the tunability of on-site potential, we vary the system parameters d_1 and d_3, ensuring $d_1 = d_3$, while keeping $d_2 = 17$ mm fixed, as shown in Fig. 9(a). First, due to the symmetry of the on-site potential, we can analytically calculate the width of these transition waves using the ϕ^6 model (see Supplemental Material [34], Sec. V, and Ref. [40] therein for details) and plot the results in Fig. 9(b). The analysis reveals that the spatial width of the colliding waves increases with increasing d_3, indicating that wave width decreases as the asymmetry of the energy wells becomes larger. We then simulate the collision of $2 \rightarrow 1$ and $2 \rightarrow 3$ transition waves.

Upon collision, we plot the steady-state displacements of the middle particles (fourth, fifth, sixth, and seventh) in a ten-particle chain, as shown in Fig. 9(c). Similarly, Fig. 9(d) illustrates the steady-state displacements of the middle particles (fourth, fifth, and sixth) in a nine-particle chain. We observe that, in general, more middle particles shift toward Phase 2 as d_3 increases. However, in odd-particle chains, the middle particle always stabilizes at Phase 2. Overall, the zone of influence, which defines the stationary domain wall formed after the collision of two transition waves, increases with
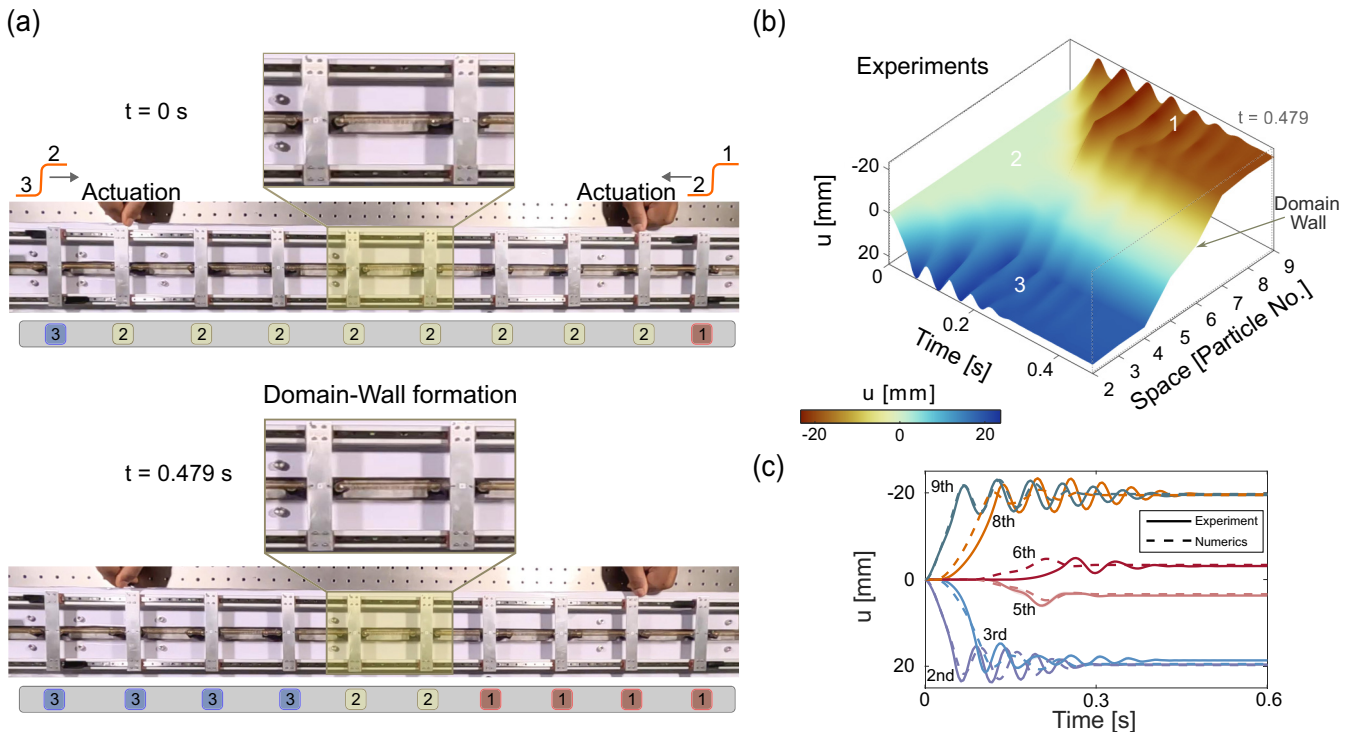

FIG. 8. Collision of two transition waves leads to a stationary domain wall. (a) Experimental snapshots highlighting the formation of the stationary domain. The unit cells are labeled with the phases. (b) Spatiotemporal plot obtained from experiments showing the formation of the stationary domain wall. (c) Displacement time series of several particles in the chain.
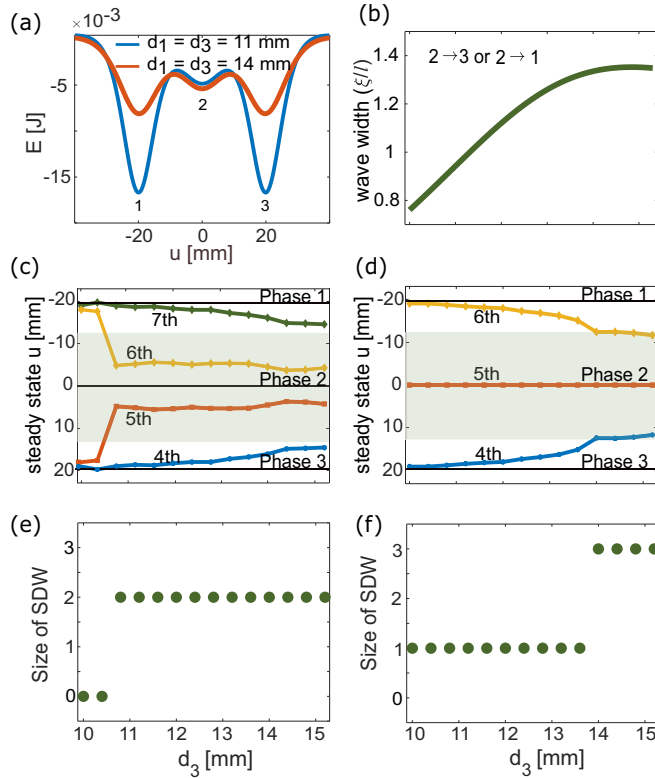
FIG. 9. (a) On-site potential for varying d_1 and d_3 keeping $d_2 = 17$ mm fixed. (b) Wave width (normalized with respect to the unit cell length l) of $2 \rightarrow 3$ or $2 \rightarrow 1$ transition wave vs d_3 derived analytically. (c) and (d) Steady-state displacements of the middle particles in the chain for even and odd lattices. (e) and (f) Size of stationary domain wall for even and odd lattices for varying d_3.

d_3. This observation aligns with the increasing wave width as d_3 grows.

To quantify the width of the stationary domain wall, we define the zone of influence as the number of unit cells in their steady state within a tolerance range of ± 12 mm around Phase 2. Figures 9(e) and 9(f) show the size of the stationary domain wall. For even-particle chains, the size increases from zero to two particles as d_3 increases, while for odd-particle chains, the size grows from one to three particles. This again highlights the correlation between the colliding wave width and the stationary domain wall width, both of which increase as d_3 increases.

Finally, similar to the ability to control the spatial location of nucleation, the location of the domain wall can be tuned by introducing a time delay in triggering the transition waves from either end [refer to Supplemental Material [34] (Sec. IV) for details].

V. CONCLUSION

In summary, we investigate a one-dimensional chain with localized external magnetic fields, formed by an assembly of permanent magnets. Specifically, our focus is on a tristable lattice, where we experimentally verify the existence of different types of transition waves. These waves sustainably propagate in the lattice due to the designed asymmetry in the potential well. We also verify experimentally a scaling law that relates the averaged power dissipated to the asymmetry in the potential well and wave velocity for all types of transition waves. We also report the reflection of transition waves from finite boundaries.

Additionally, we explore the collision of transition waves. In the case of an asymmetric potential well, when two transition waves collide as a kink and antikink, we observe experimentally the remote nucleation of a new phase. We report the occurrence of nucleation for a range of asymmetry in tristable potential. For larger asymmetry, nucleation is accompanied by propagation due to the large kinetic energy of nucleating particles. However, in the case of a symmetric potential well, two transition waves collide as kinks, resulting in the formation of a stationary domain wall between two different phases. We show the width of the stationary domain wall can be tuned by the shape of the tristable potential, which also dictates the width of the colliding transition waves.

These findings underscore the richness of dynamical phenomena in multistable lattices. The design holds promise for the development of reconfigurable materials under external fields, where remote actuation through transition waves can be utilized to tune the final state of the material.

Future work will focus on extending these findings to higher-dimensional systems. Additionally, it would be intriguing to explore whether similar tunability can be achieved by modifying intersite potentials instead of on-site potentials, as investigated in this study. Preliminary analysis (see Supplemental Material [34], Sec. VI) indicates that intersite multistability leads to transitions occurring in the strains of the connecting springs rather than their displacements.

[1] O. M. Braun and Y. S. Kivshar, *The Frenkel-Kontorova Model: Concepts, Methods, and Applications* (Springer, New York, 2004).

[2] J. F. Currie, A. Blumen, M. A. Collins, and J. Ross, Dynamics of domain walls in ferrodistortive materials II. Applications to Pb$_5$Ge$_3$O$_{11}$- and SbSi-type ferroelectrics, Phys. Rev. B **19**, 3645 (1979).

[3] D. Atkinson, D. A. Allwood, G. Xiong, M. D. Cooke, C. C. Faulkner, and R. P. Cowburn, Magnetic domain-wall dynamics in a submicrometre ferromagnetic structure, Nat. Mater. **2**, 85 (2003).

[4] F. Falk, Ginzburg-Landau theory and solitary waves in shape-memory alloys, Z. Phys. B **54**, 159 (1984).

[5] M. Remoissenet and M. Peyrard, Soliton dynamics in new models with parametrized periodic double-well and asymmetric substrate potentials, Phys. Rev. B **29**, 3153 (1984).

[6] J. Pouget and G. A. Maugin, Solitons and electroacoustic interactions in ferroelectric crystals. II. Interactions of solitons and radiations, Phys. Rev. B **31**, 4633 (1985).

[7] R. Abeyaratne and J. K. Knowles, Kinetic relations and the propagation of phase boundaries in solids, Arch. Ration. Mech. Anal. **114**, 119 (1991).

[8] M. Peyrard, Simple theories of complex lattices, Phys. D (Amsterdam, Neth.) **123**, 403 (1998).

[9] S. Flach, Y. Zolotaryuk, and K. Kladko, Moving lattice kinks and pulses: An inverse method, Phys. Rev. E **59**, 6105 (1999).

[10] L. Slepyan and M. Ayzenberg-Stepanenko, Localized transition waves in bistable-bond lattices, J. Mech. Phys. Solids **52**, 1447 (2004).

[11] L. Slepyan, A. Cherkaev, and E. Cherkaev, Transition waves in bistable structures. II. Analytical solution: Wave speed and energy dissipation, J. Mech. Phys. Solids **53**, 407 (2005).

[12] L. Truskinovsky and A. Vainchtein, Kinetics of martensitic phase transitions: Lattice model, SIAM J. Appl. Math. **66**, 533 (2005).

[13] I. Benichou and S. Givli, Structures undergoing discrete phase transformation, J. Mech. Phys. Solids **61**, 94 (2013).

[14] N. Nadkarni, A. F. Arrieta, C. Chong, D. M. Kochmann, and C. Daraio, Unidirectional transition waves in bistable lattices, Phys. Rev. Lett. **116**, 244501 (2016).

[15] B. Deng, J. R. Raney, K. Bertoldi, and V. Tournat, Nonlinear waves in flexible mechanical metamaterials, J. Appl. Phys. **130**, 040901 (2021).

[16] B. Deng, L. Chen, D. Wei, V. Tournat, and K. Bertoldi, Pulse-driven robot: Motion via solitary waves, Sci. Adv. **6**, 18 (2020).

[17] Y. Chi, Y. Li, Y. Zhao, Y. Hong, Y. Tang, J. Yin, Y. Chi, Y. Li, Y. Zhao, Y. Hong, J. Yin, and Y. Tang, Bistable and multistable actuators for soft robots: Structures, materials, and functionalities, Adv. Mater. **34**, 2110384 (2022).

[18] S. Shan, S. H. Kang, J. R. Raney, P. Wang, L. Fang, F. Candido, J. A. Lewis, K. Bertoldi, S. Shan, S. H. Kang, J. R. Raney, P. Wang, L. Fang, F. Candido, J. A. Lewis, and K. Bertoldi, Multistable architected materials for trapping elastic strain energy, Adv. Mater. **27**, 4296 (2015).

[19] A. Zareei, B. Deng, and K. Bertoldi, Harnessing transition waves to realize deployable structures, Proc. Natl. Acad. Sci. USA **117**, 4015 (2020).

[20] V. Ramakrishnan, . M. J. Frazier, and M. J. Frazier, Multistable metamaterial on elastic foundation enables tunable morphology for elastic wave control, J. Appl. Phys. **127**, 225104 (2020).

[21] A. A. Watkins, A. Eichelberg, and O. R. Bilal, Exploiting localized transition waves to tune sound propagation in soft materials, Phys. Rev. B **104**, L140101 (2021).

[22] N. Nadkarni, C. Daraio, and D. M. Kochmann, Dynamics of periodic mechanical structures containing bistable elastic elements: From elastic to solitary wave propagation, Phys. Rev. E **90**, 023204 (2014).

[23] J. R. Raney, N. Nadkarni, C. Daraio, D. M. Kochmann, J. A. Lewis, and K. Bertoldi, Stable propagation of mechanical

signals in soft media using stored elastic energy, Proc. Natl. Acad. Sci. USA **113**, 9722 (2016).

[24] S. Katz and S. Givli, Solitary waves in a bistable lattice, Extreme Mech. Lett. **22**, 106 (2018).

[25] I. Shiroky and O. Gendelman, Propagation of transition fronts in nonlinear chains with non-degenerate on-site potentials, Chaos **28**, 023104 (2018).

[26] B. Deng, P. Wang, V. Tournat, and K. Bertoldi, Nonlinear transition waves in free-standing bistable chains, J. Mech. Phys. Solids **136**, 103661 (2020).

[27] W. Zhou and Y.-Z. Wang, Cooperative propagation and directional phase transition of topological solitons in multi-stable mechanical metamaterials, J. Mech. Phys. Solids **175**, 105287 (2023).

[28] H. Yasuda, L. M. Korpas, and J. R. Raney, Transition waves and formation of domain walls in multistable mechanical metamaterials, Phys. Rev. Appl. **13**, 054067 (2020).

[29] H. Yasuda, H. Shu, W. Jiao, V. Tournat, and J. R. Raney, Nucleation of transition waves via collisions of elastic vector solitons, Appl. Phys. Lett. **123**, 051701 (2023).

[30] L. Jin, R. Khajehtourian, J. Mueller, A. Rafsanjani, V. Tournat, K. Bertoldi, and D. M. Kochmann, Guided transition waves in multistable mechanical metamaterials, Proc. Natl. Acad. Sci. USA **117**, 2319 (2020).

[31] B. Deng, S. Yu, A. E. Forte, V. Tournat, and K. Bertoldi, Characterization, stability, and application of domain walls in flexible mechanical metamaterials, Proc. Natl. Acad. Sci. USA **117**, 31002 (2020).

[32] A. Pal and M. Sitti, Programmable mechanical devices through magnetically tunable bistable elements, Proc. Natl. Acad. Sci. USA **120**, e2212489120 (2023).

[33] N. Nadkarni, C. Daraio, R. Abeyaratne, and D. M. Kochmann, Universal energy transport law for dissipative and diffusive phase transitions, Phys. Rev. B **93**, 104109 (2016).

[34] See Supplemental Material at http://link.aps.org/supplemental/10.1103/PhysRevMaterials.9.014405 for the detailed calculation of on-site potential, transition waves and their collision in longer chains, analytical solutions, and discussion on the case with tristable intersite potential.

[35] R. D. James and S. Müller, Internal variables and fine-scale oscillations in micromagnetics, Continuum Mech. Thermodyn. **6**, 291 (1994).

[36] J. Cui, J. Ormerod, D. Parker, R. Ott, A. Palasyuk, S. Mccall, M. P. Paranthaman, M. S. Kesler, M. A. McGuire, I. C. Nlebedim et al., Manufacturing processes for permanent magnets: Part I—Sintering and casting, JOM **74**, 1279 (2022).

[37] M. Remoissenet, *Waves called Solitons: Concepts and experiments* (Springer, Berlin, Heidelberg, 2013).

[38] W. Jiao, H. Shu, V. Tournat, H. Yasuda, and J. R. Raney, Phase transitions in 2D multistable mechanical metamaterials via collisions of soliton-like pulses, Nat. Commun. **15**, 333 (2024).

[39] A. Paliovaios, G. Theocharis, V. Achilleos, and V. Tournat, Transition waves in bistable systems generated by collision of moving breathers, Extreme Mech. Lett. **71**, 102199 (2024).

[40] A.-M. Wazwaz, Compactons, solitons and periodic solutions for some forms of nonlinear Klein–Gordon equations, Chaos, Solitons Fract. **28**, 1005 (2006).